
**This manuscript has been published in EARTH AND SPACE SCIENCE.
Please refer to the 'Peer-reviewed Publication DOI' link on the right-hand side of this webpage for the
final version of this manuscript.**

Evaluation of Vegetation Bias in InSAR Time Series for Agricultural Areas within the San Joaquin Valley, CA

Kelly R. Devlin¹ and Rowena B. Lohman¹

¹Department of Earth and Atmospheric Sciences, Cornell University, Ithaca, NY.

Corresponding author: Kelly R. Devlin (krd86@cornell.edu)

Key Points:

- We quantify the contribution of bias from vegetation and soil moisture effects on InSAR phase and time series
- We find biases of ~2-4 cm/yr within agricultural fields, with the largest biases occurring in cotton fields within Tulare Lake basin
- We suggest removing agricultural fields from time series analysis can help mitigate phase biases

Abstract

Agricultural regions present a particularly difficult set of challenges during interferometric synthetic aperture radar (InSAR) displacement time series analyses due to the existence of abrupt transitions in land use over short spatial scales and rapid temporal changes associated with different stages of the agricultural cycle. Plant growth and soil moisture changes can introduce phase biases within interferograms that could be misinterpreted as displacement. We analyze a full-resolution, multi-year SAR time series over California's San Joaquin Valley, an intensively cultivated region producing a wide variety of crops. Using independent information about land cover and crop type, we isolate the effects of individual crops on backscatter amplitude, interferometric phase change, and interferometric coherence over space and time. We determine the temporal behavior of the phase changes associated with several key crop types by isolating the difference between the phase of pixels averaged over each agricultural field and the phase values of pixels in nearby roads and developed areas. We find that some fields are associated with a bias of ~2-4 cm/yr of apparent subsidence, with strong seasonal variability in the degree of bias. When InSAR imagery is spatially averaged or filtered, these biases also impact the inferred phase in nearby roads and other land cover types. We show that even a simple approach, where pixels associated with agricultural fields are removed or masked out before further processing, can mitigate the crop-related biases that we observe in the study area.

Plain Language Summary

We examine maps of ground displacement over the San Joaquin Valley, CA, which contains a variety of crop types. We use information about ground cover and crop type to isolate the average effects of individual agricultural fields. We find that some fields can lead to an overestimation of subsidence by about 2-4 cm/yr. It is important to understand the effect of agricultural activity on displacement maps in order to accurately interpret where and how fast subsidence is occurring. Even something as simple as removing the agricultural fields from the data at an early stage, before interpretation, can remove these false signals.

1 Background

Many intensively cultivated agricultural regions around the world are heavily reliant on groundwater extraction. Groundwater overdraft is a widely recognized problem globally, with numerous large aquifers being depleted faster than they can recharge (e.g., Gleeson et al., 2012; Richey et al., 2015; Wada et al., 2010). The adverse effects of groundwater overdraft include saltwater intrusion, damage to ecosystems, land subsidence, and permanent aquifer storage loss (e.g., Asner et al., 2016; Hasan et al., 2023; Nishikawa et al., 2009; Rohde et al., 2024).

One place where the effects of groundwater extraction have been particularly well-documented is in the San Joaquin Valley, California. The San Joaquin Valley produces over half of California's agricultural output, employs about 340,000 people, and generates over \$24 billion each year in revenue (Escriva-Bou et al., 2023). Continued, market-driven expansion of crops, particularly perennial orchards, is increasing the likelihood of frequent water shortages

in the future (Mall and Herman, 2019). Groundwater is increasingly relied on during times of drought, which further exacerbates the unsustainability of current water management practices and policy (Escriva-Bou et al., 2020; Petersen-Perlman et al., 2022). Future efforts to improve water management practices and policies will require reliable estimates of the amount and distribution of groundwater withdrawal (Butler et al., 2020). Accurate maps of land subsidence are one type of observation that can contribute to our understanding of the groundwater budget for this and other aquifers around the world.

Land subsidence in the San Joaquin Valley due to groundwater overdraft has been recorded for decades, with the first geodetic observations in the 1920s (Poland et al., 1975). Since the 1990s, interferometric synthetic aperture radar (InSAR) has been used to study ground displacements due to a range of subsurface processes (e.g., Massonnet et al., 1993), including subsidence associated with the extraction of groundwater (e.g., Amelung et al., 1999; Chaussard et al., 2014; Gao et al., 2018; Hussain et al., 2022; Motagh et al., 2017). Numerous studies document subsidence in the San Joaquin Valley using InSAR, GPS, and ground truth measurement (e.g., Farr, 2016; Kang and Knight, 2023; Murray and Lohman, 2018; Neely et al., 2020). Inferred subsidence rates were as high as 30 cm/yr during the 2012-2016 California drought. However, InSAR observations are also impacted by factors that are not accounted for in most analyses, such as vegetation and soil moisture (e.g., Dall, 2007; De Zan and Gomba, 2018; Gabriel et al., 1989; Zheng et al., 2022; Zwieback et al., 2015).

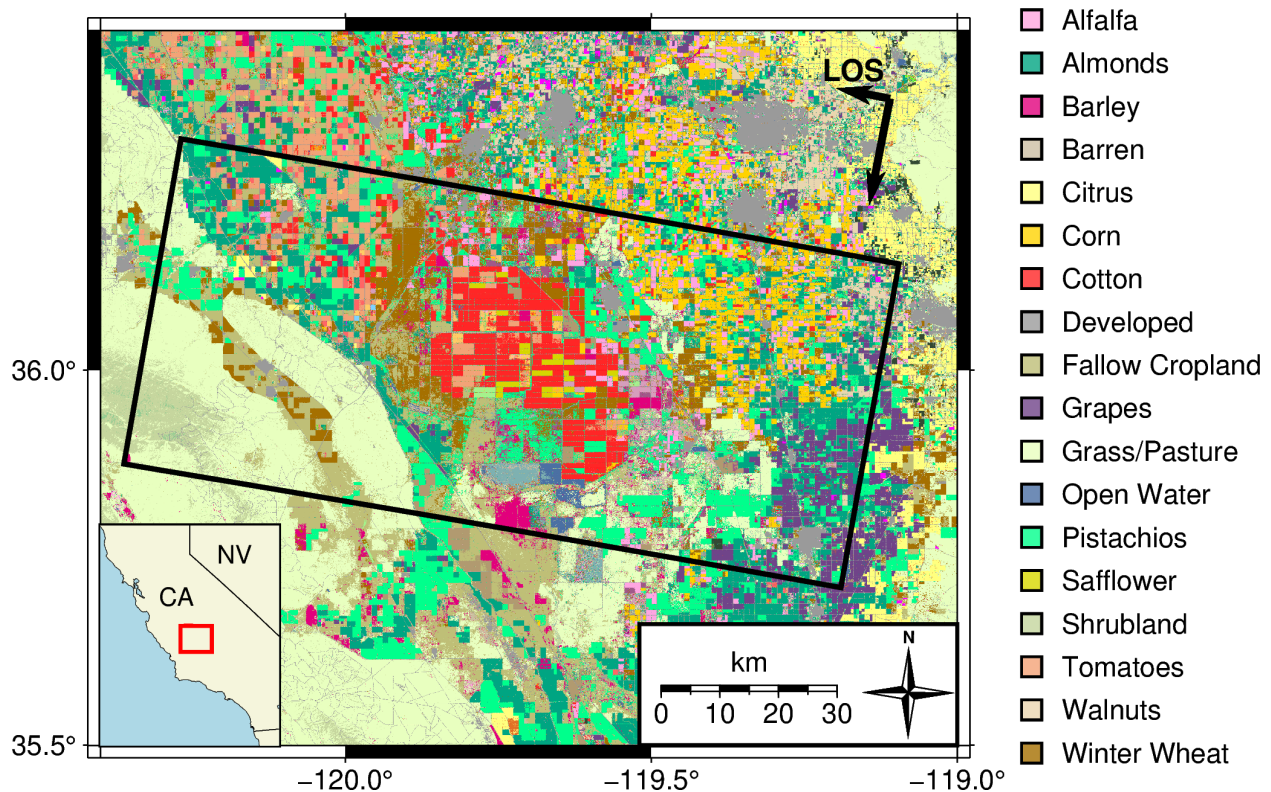


Figure 1. Location of study site within San Joaquin Valley, CA (inset, panel location indicated with red rectangle). Colors indicate crop and ground cover type in 2020 based on USDA Cropland Data Layer database (USDA NASS, 2021). Black box outlines extent of SAR footprint

(subset of Sentinel-1a/b Descending Track 144). We use 129 SAR acquisitions from 08/2019 - 09/2021 with 6 day repeats

In this study, we evaluate potential phase biases due to contributions from cropland over the southern San Joaquin Valley (Figure 1). We compare the InSAR phase averaged over individual fields with the phase of nearby roads and stable surfaces. This approach allows us to separate the effect of crop growth, irrigation and other agricultural activities that vary on the spatial scale of individual fields from the much larger spatial scale features associated with aquifer-related subsidence and tropospheric variability. In Section 2, we describe the datasets used in our analysis. In Section 3, we briefly discuss geophysical factors that affect InSAR phase and describe our method for calculating the phase bias associated with individual fields as well as the resulting displacement time series and inferred velocity map. In Section 4, we report the results of our methodology, including the behavior of specific crops over time and the results of our two different types of velocity inversions. Finally, in Section 5, we discuss the fields and crops that have the largest biases. We comment on the potential overestimation of subsidence in InSAR time series and provide recommendations on the appropriate strategy for dealing with these biases.

2 Data

We use freely available C-band SAR imagery from descending Track 144 of the European Space Agency's Sentinel-1a/b mission acquired between 2019/08/14 and 2021/09/20 on a 6-day repeat interval (129 acquisitions). We use crop information between 2019 and 2021 from the Cropland Data Layer (CDL) created by the United States Department of Agriculture (USDA), National Agricultural Statistics Service (USDA NASS, 2021). The CDL is a freely available geospatial dataset of Land Cover Land Use Change (LCLUC) and crop classification offered at annual intervals at 30-m pixel resolution derived from remotely-sensed data. The current CDL Program uses the Landsat 8 and 9 OLI/TIRS sensor, the Disaster Monitoring Constellation (DMC) DEIMOS-1 and UK2, the ISRO ResourceSat-2 LISS-3, and the ESA SENTINEL-2 A and B sensors (USDA NASS, 2021).

We use Google Earth Engine (Gorelick et al., 2017) to obtain Landsat 8 Surface Reflectance imagery courtesy of the U.S. Geological Survey and Sentinel-2 MSI: MultiSpectral Instrument, Level-2A imagery (Copernicus Sentinel-2 (processed by ESA), 2021) acquired between 2019/08/15 and 2021/09/23 (205 acquisitions). Landsat 8 and Sentinel-2 imagery are available at 30-m and 10-m pixel resolutions, respectively. We use these Landsat 8 and Sentinel-2 optical imagery to calculate normalized difference vegetation index (NDVI) within each field. NDVI is defined as:

$$NDVI = \frac{NIR - RED}{NIR + RED} \quad (1)$$

where NIR is the observed reflectance of the near-infrared band and RED is the observed reflectance of the red band. NDVI values are, by definition, bounded within the range $[-1,1]$, with higher values generally indicating healthier or denser vegetation.

3 Methods

In this section, we review standard terminology used in interferogram analysis, then describe our InSAR processing workflow, from individual interferograms through time series analysis (Figure 2). The phase of a full-resolution, unfiltered interferogram can be expressed (modulo 2π) as:

$$\varphi_{ifg} = \varphi_{disp} + \varphi_{atm} + \varphi_{topo} + \varphi_{srf} + \varphi_{other} \quad (2)$$

where φ_{ifg} is the phase of the interferogram, φ_{disp} is the ground displacement vector projected onto the satellite's line-of-sight (LOS), φ_{atm} is the atmospheric delay, φ_{topo} is from digital elevation model (DEM) errors, φ_{srf} is the contribution from surface properties, such as soil moisture, vegetation, and their temporal changes, and φ_{other} includes all other noise sources such as thermal and decorrelation noise (Zebker and Villasenor, 1992). Below, we refer to φ_{srf} as the “bias” to our time series, which assumes that the goal is to extract information about deformation associated with deeper earth processes. φ_{srf} on its own is also potentially a signal of interest, due to real physical changes in soil and vegetation properties.

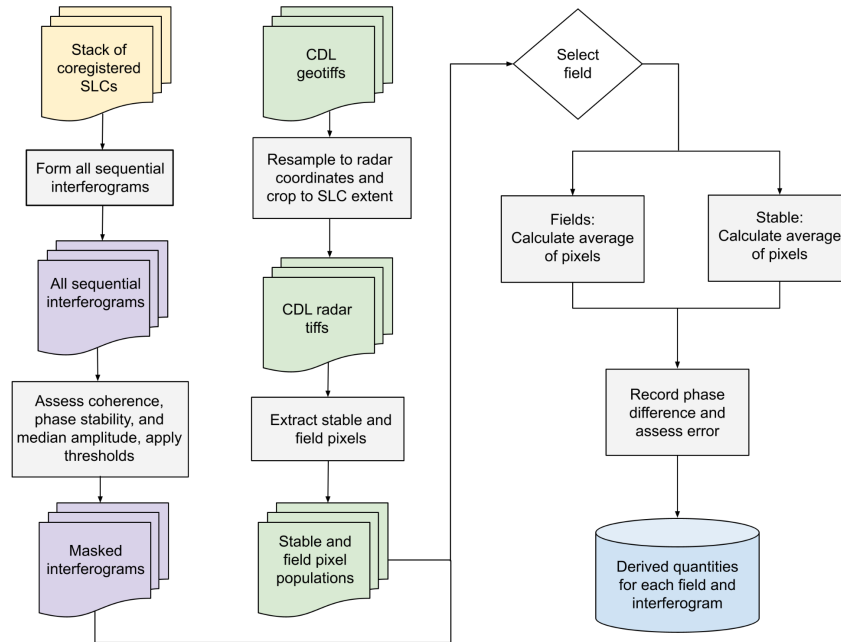


Figure 2. Workflow from raw data to interferograms for individual fields. Colors indicate CDL and CDL-derived products (green), coregistered SLCs (yellow), complex-valued products from

InSAR (purple), and the final dataset with derived quantities for each field and interferogram (blue). Gray rectangles represent manipulation of datasets and white diamond represents selection of chosen crop for masking. Parallel lines indicate identical steps taken on both interferogram stacks independently.

For this study, we focus on isolating φ_{srf} from the other factors and evaluating phase contributions associated with a given crop type. To isolate φ_{srf} , we rely on the assumption that φ_{disp} and φ_{atm} have spatial scales that are large relative to the size of individual agricultural fields (Emardson et al., 2003), and we also assume that φ_{other} is random in time with mean zero and will introduce a negligible contribution to our final time series. Because the San Joaquin Valley has very low topographic variation, we also neglect consideration of φ_{topo} in this work. We isolate φ_{srf} at any location in a given interferogram by taking the difference in phase between an agricultural field and any adjacent roads and other developed areas (Section 3.2), under the assumption that they will have less sensitivity to soil and vegetation moisture changes than the agricultural fields.

To assess and control for data quality, we use several metrics. The first is the interferometric complex coherence, γ , defined as:

$$\gamma = \frac{\langle ab^* \rangle}{\sqrt{\langle aa^* \rangle \langle bb^* \rangle}} \quad (3)$$

where a is the first SAR acquisition, b is the second SAR acquisition, $*$ denotes the complex conjugate, and $\langle \cdot \rangle$ denotes a spatial average. We use the complex coherence magnitude, $|\gamma|$, (simply referred to “coherence”, below) which falls in the range [0,1]. Low values of coherence (decorrelation) are associated with more phase variability within the spatial averaging window, and high values of coherence indicate data that is more uniform over that scale. In the San Joaquin Valley, we expect decorrelation when there are rapid changes in vegetation and soil moisture properties between two SAR acquisitions, such as during times of tilling, irrigation, crop growth, and harvesting. During these time periods, the phase values have little physical meaning and appear as uniform random noise within any fields associated with these activities.

Another metric of data quality we used is the phase stability, χ , similar to (Hooper et al., 2004), which is defined as:

$$\chi = \frac{1}{n-1} \left| \sum_{i=1}^{n-1} \exp \{ j(\varphi_{i,i+1} - \langle \varphi_{i,i+1} \rangle) \} \right| \quad (4)$$

where n is the number of SAR acquisitions, $\varphi_{i,i+1}$ and $\langle \varphi_{i,i+1} \rangle$ are the unfiltered and filtered phase for interferogram between dates i and $i+1$, respectively. $\langle \varphi_{i,i+1} \rangle$ is calculated by taking the argument of the spatial average of the interferogram; we perform our calculation over a window with 4 pixels in azimuth and 20 in range. Similar to coherence, phase stability falls in

the range [0,1]. Low phase stability values indicate that a pixel's behavior is temporally inconsistent with its neighbors within the spatial averaging window. Conversely, high phase stability values indicate that a pixel's behavior is temporally consistent with its neighbors. Below, when we discuss operations on single interferograms, we drop the i and $i+1$ notation for brevity.

3.1 SAR imagery preparation

We generate a full-resolution coregistered series of single look complex (SLC) imagery using the open-source InSAR Scientific Computing Environment version 2 (ISCE2) (Rosen et al., 2012) and the Sentinel stack processor (Fattahi et al., 2017). We remove topographic effects using the Shuttle Radar Topography Mission (SRTM) DEM (Farr et al., 2007). We use our coregistered SLC stack to generate 128 sequential six day full-resolution interferograms. We apply several thresholds to mask out unreliable pixels. We mask out pixels with coherence ≤ 0.3 in each interferogram. We mask out all pixels with median amplitude ≤ 34 dB over all dates. This removes pixels within the Tule River, which is immediately adjacent to several of the roads in our study site. Additionally, we mask out all pixels with phase stability ≤ 0.4 to only include pixels that behave similarly to their neighbors when averaged over the entire study period. For our analysis below, we resample CDL products and NDVI products onto the range-doppler coordinate system of the original, full-resolution SLC imagery. When we directly compare NDVI to InSAR observations, we interpolate the NDVI time series onto the dates of the SAR imagery.

3.2 Field-specific analysis

Our goal is to compare the average interferometric phase of each individual field with the average interferometric phase of nearby roads and other stable surfaces. To identify individual fields, we select all pixels labeled in the CDL as one of six crops (almonds, cotton, grapes, pistachios, tomatoes, and winter wheat) any year between 2019 and 2021. We perform a series of morphological operations based on bitmaps of the distribution of each crop (e.g., “erode” and “dilate” with OpenCV (Bradski, Gary, 2000)). Specifically, we use a 10 azimuth x 5 range kernel to erode over seven iterations and dilate over six iterations. This process reduces the number of isolated pixels within and around each field. We then identify the connected components based on the resulting bitmap associated with each crop. We assign each individual field an identification number. This process identifies 3167 agricultural fields that cover 26% of the total area of our study site (Figure S1a). To identify roads and other stable surfaces, we select all pixels labeled in the CDL as developed or barren at any point between 2019 and 2021. These pixels cover 7% of the total area of our study site (Figure S1b).

We track several metrics for each field within each interferogram: SLC backscatter amplitude, average phase bias per field (φ_{bias}), and coherence (γ). We define average phase

bias as the difference between the average phase within a single field (φ_{field}) and the average phase of the surrounding stable pixels within 100 m (φ_{stable}) (Figure 2):

$$\varphi_{bias} \equiv \arg(\exp\{j(\bar{\varphi}_{field} - \bar{\varphi}_{stable})\}) \quad (5)$$

3.3 Time series analyses

To quantify the contribution of phase biases within agricultural fields on displacement time series, we perform two types of time series analysis - one where we compare the results of using masked vs. unmasked versions of the real interferograms, and one where generate synthetic interferograms based on the phase estimates for each field and time interval as described in Section 3.2.

3.3.1 Masked vs. unmasked real-data time series

As described above, the study area is marked by very heterogeneous land cover, with sparse networks of roads, few cities, and natural terrain, interspersed between large agricultural fields. The roads are narrow relative to the filtering and spatial averaging scales that are typically used in InSAR processing, so their interferometric phase will tend to be “corrupted” by the phase in the adjacent fields during most InSAR processing workflows. To assess the potential impact of filtering/averaging over a mix of stable and agricultural pixels, we perform two time series analyses - one with the original set of interferograms and one where we mask out all but the stable pixels (as described in Section 3.2) at the highest resolution before any further processing.

We use the spatial resolutions and filtering choices used in the JPL-Caltech Advanced Rapid Imaging and Analysis (ARIA) project (Bekaert et al., 2019), which provides a free and open archive of Sentinel-1 unwrapped geocoded interferogram products. We spatially average the full resolution wrapped interferograms by a factor of 19 in the range direction and 7 in the azimuth direction, resulting in pixels that are approximately 90 m in scale. For the “masked” version of the dataset, only the unmasked pixels are used in this spatial averaging. In places where there are no unmasked pixels within the 19x7 spatial averaging window, the spatially averaged, masked interferogram is undefined. For the unmasked interferograms, we apply a Goldstein-Werner filter with $\alpha = 0.1$ (Goldstein and Werner, 1998), then unwrap the interferograms using SNAPHU (Chen and Zebker, 2002), resulting in the filtered, unwrapped version of the unmasked phase, φ_{unw}^{unmask} .

Filtering and unwrapping the masked interferograms is more challenging because of the undefined/masked values present within each interferogram. We address this by assuming that, within the set of stable pixels, the difference between the unwrapped, unfiltered phase values and the unwrapped, filtered phase values in the unmasked dataset, φ_{unw}^{unmask} , should fall within the range $[-\pi, \pi]$. This would not necessarily be true in the presence of very large amounts of noise (in which case unwrapping will likely fail in both cases) or where the spatial

scale of filtering is large relative to the gradients in strain present in the interferogram. Where this assumption holds, the 2π phase ambiguity needed to define the unwrapped, masked interferometric phase, φ_{unw}^{mask} , can be solved for (e.g., Jiang and Lohman, 2021; Tymofyeyeva et al., 2019):

$$\varphi_{unw}^{mask} = \arg(\exp\{j(\Delta\varphi_{i,i+1})\}) + \varphi_{unw}^{unmask} \quad (6)$$

where $\Delta\varphi_{i,i+1}$ is the difference in phase between the spatially averaged, filtered, unwrapped wrapped interferogram, between dates i and $i+1$, and the spatially averaged, masked, wrapped interferogram (Figure S2). As mentioned above, we expect the value of $\Delta\varphi_{i,i+1}$ to fall within the range $[-\pi, \pi]$ due to the small size of the filtering/spatial averaging window with respect to the scale of variations in atmospheric noise or strain due to aquifer depletion. The largest values of $\Delta\varphi_{i,i+1}$ will occur in areas over heterogeneous terrain, such as at the boundaries between fields and nearby stable pixels. We see consistent offsets over many interferograms between the roads and fields that are well below 2π (Section 4), suggesting that the spatial averaging/filtering across these boundaries does not introduce more than one cycle.

We produce displacement time series and inferred average displacement rates using the standard workflow from open source Miami INsar Time-series software in PYthon (MintPy) (Yunjun et al., 2019). We use the same reference pixel for each inversion and use the sign convention such that subsidence is associated with a negative velocity in the LOS direction. We apply this approach to both the sets of interferograms and compare the results in Section 4.

3.3.2 Synthetic time series, based on observed field biases

Our goal is to understand how the history of phase biases, φ_{bias} , described in Section 3.2, affect the displacement time series inferred from a given set of interferograms. To assess this, we need to simulate how the standard processes of filtering, spatial averaging, and phase unwrapping perform in the presence of these phase biases. Therefore, we generate synthetic data that include the phase biases observed in the real data for each field and for each interferogram (Figure 3), and process them in the same way that we would treat real interferograms. We begin by constructing synthetic full-resolution wrapped interferograms. For each interferogram, we assign the φ_{bias} observed from the real interferogram for each field.

We then introduce Gaussian noise scaled to be consistent with the coherence γ of the actual interferogram:

$$\sigma = \sqrt{-2 \ln \gamma} \quad (7)$$

where σ is the standard deviation and γ is the absolute value of the complex coherence in Eq. 4. After generating these full-resolution synthetic interferograms, we process them and infer velocity using the same workflow as we used for the real data as described in Section 3.3.1.

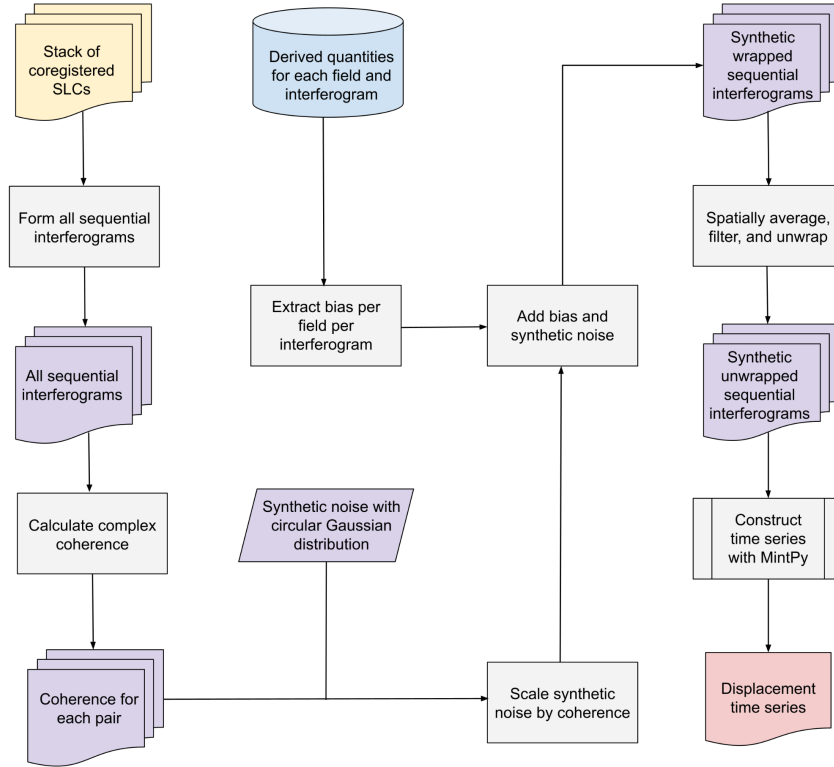


Figure 3. Workflow for synthetic time series. Colors indicate coregistered SLCs (yellow), complex-valued datasets from InSAR (purple), CDL and CDL-derived products (green), average phase bias calculated in Figure 2 (blue), and final synthetic displacement time series (red). Gray rectangles represent processes to manipulation of datasets, and white diamond represents determination of whether each field is sufficiently coherent. Details of MintPy are described in (Yunjun et al., 2019).

4 Results

4.1 Relationship between phase bias and crop type

Our analysis includes 3167 individual fields that are flagged in the CDL database as one of the six crops we focus on (almonds, cotton, grapes, pistachios, tomatoes, and winter wheat).

Figure 4 shows an example of the sharp phase transitions at field boundaries that are present throughout this dataset.

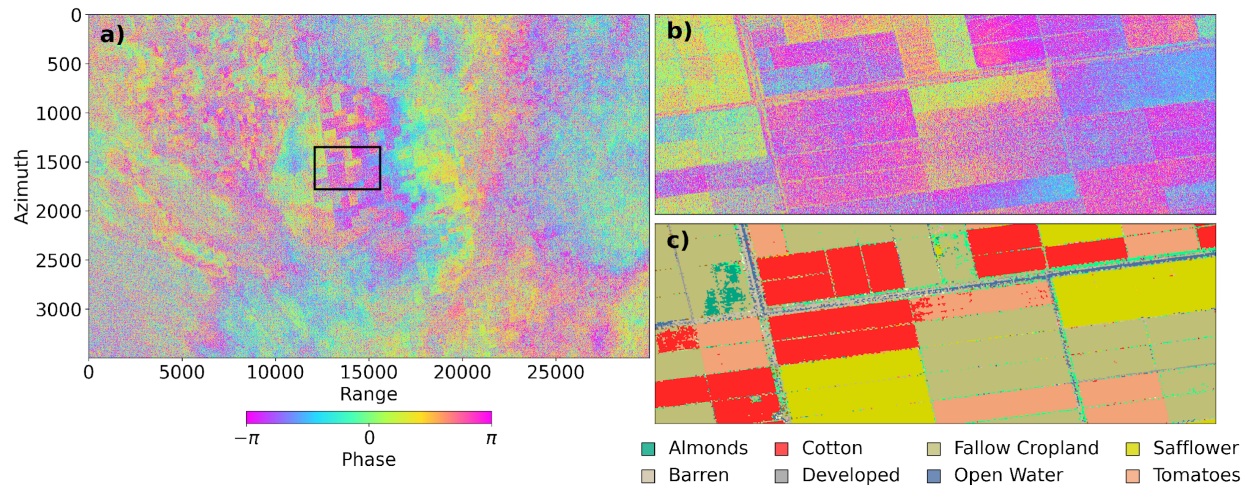


Figure 4. (a) Six-day full-resolution wrapped interferogram between 2021-01-23 and 2021-01-29 of the entire study region in radar coordinates. Black box outlines zoomed in subregion of (b); (b) Subregion of (a) showing sharp contrast between fields and adjacent roads. Interferogram is wrapped on $[-\pi, \pi]$ interval; (c) CDL in radar coordinates in with the eight most common land cover types of subregion (b).

Figure 5 shows phase bias over time for each crop type. In each panel, the phase bias is shown for each field of that crop type, for each interferogram, except for when $<10\%$ of the pixels in that field or in the surrounding “stable” pixels had coherence > 0.3 . Cotton is associated with the largest average phase bias and a strong seasonality. Cotton and tomato fields are heavily decorrelated between July and September. The other four crops are coherent for the majority of our time frame. Almonds and pistachios also are associated with a clear

seasonal phase bias, without the annual loss of coherence observed within the cotton fields. Grapes, tomatoes, and winter wheat have small to negligible phase bias.

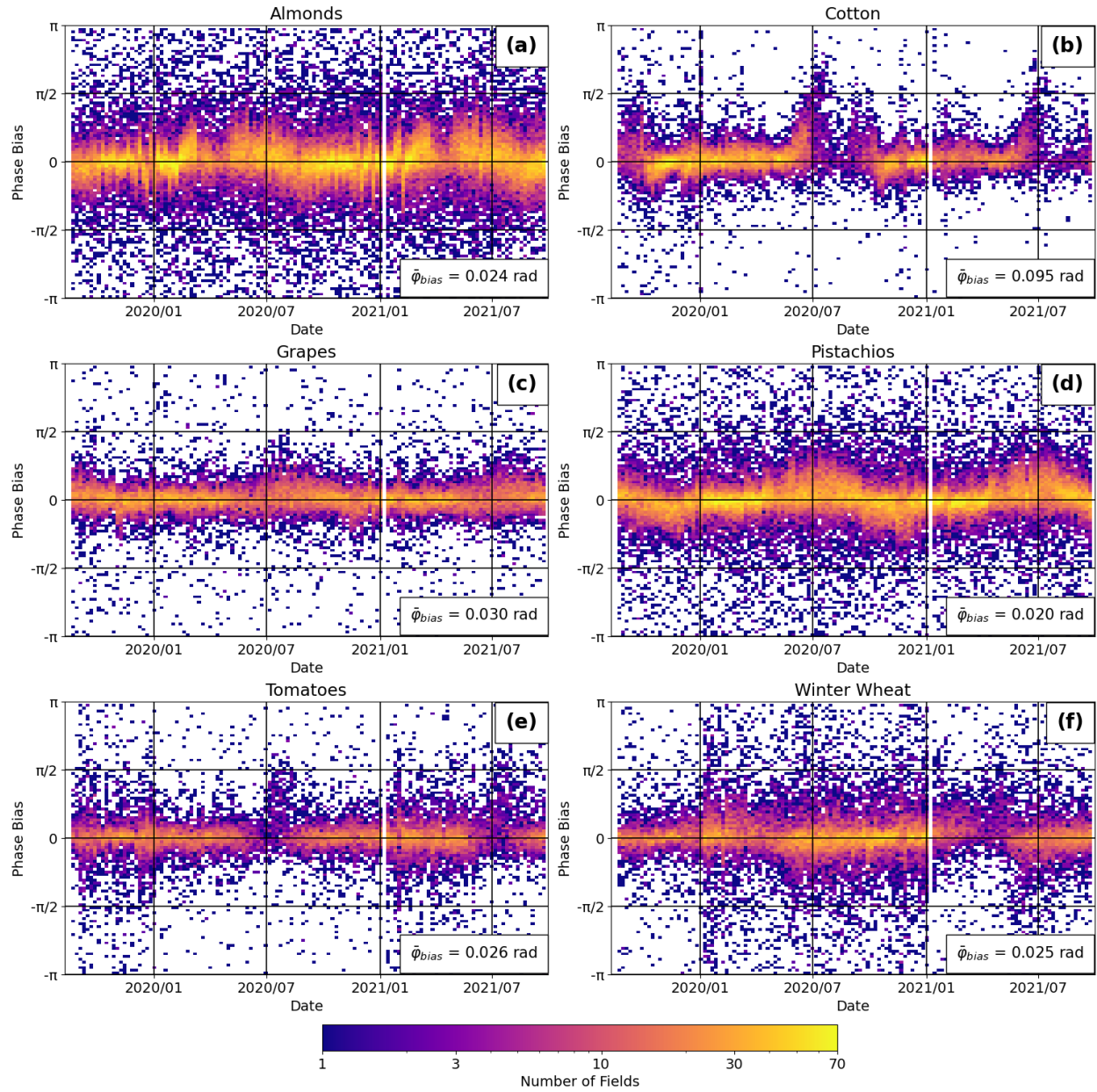


Figure 5. Heatmap of phase bias over time for each crop type. Each heatmap only includes biases at times when at least 10% of possible field and road pixels have coherence > 0.3 . Text in lower right corner indicates the mean over the full time period used in this study. Note that

this value, particularly for crops like cotton that demonstrate a large seasonality, is very sensitive to the exact time period used.

4.2 NDVI and phase bias

In this section we compare the temporal behavior of NDVI averaged over each field with the average phase bias. NDVI is a completely independent observation type and helps to illustrate the correspondence between the temporal variations in phase bias and phenological stage. Here we show the comparison against cotton, but other crop type comparisons can be found in the supplemental material. Rising NDVI values near the end of each year coincide with an increase in phase bias, followed by a time period of decorrelation when NDVI values are at a maximum (Figure 6). We observe this relationship in individual fields (Figure S3) as well as on average across all cotton fields. This indicates that the large phase biases we observe in cotton are associated with a time period where the cotton plants are beginning to grow, but the fields become decorrelated during the time period of peak vegetation density, as indicated by the peak in NDVI.

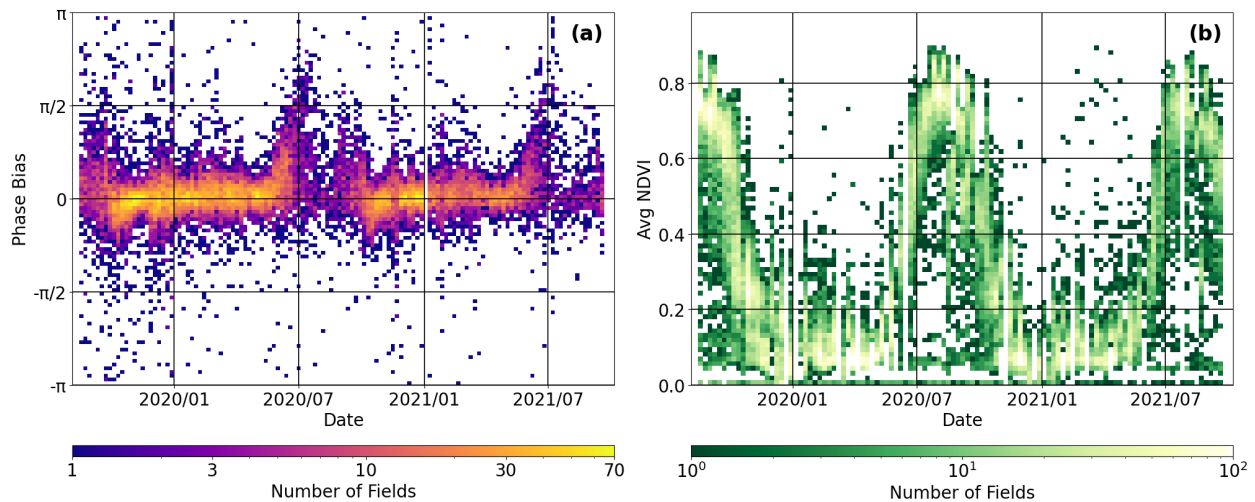


Figure 6. a) Phase bias heatmap of cotton fields over time; **b)** NDVI heatmap of cotton fields over time.

Tomatoes and winter wheat also have strong seasonal NDVI cycles, but their phase biases do not show similar temporal behavior (Figures S7, S8). The NDVI of almonds (Figure S4), grapes (Figure S5), and pistachios (Figure S6) behave similarly over time. For these three crops, some fields follow a seasonal cycle between high and low NDVI, but there are also many fields that have low NDVI during the entirety of our study period. The phase bias in some individual almond and pistachio fields coincide with NDVI seasonality, but we do not see such similarities when averaging across all fields of each respective crop. We do not observe similarities between NDVI and phase bias in grape fields. Note that all figures showing NDVI over time

include all fields containing the specific crop. Some of these fields are too decorrelated to include in our phase bias analysis.

4.3 Time series inversion results

4.3.1 Real-data time series results

As described above, many current workflows for generating InSAR time series products (e.g., Bekaert et al., 2019) include some component of spatial filtering in their analysis. In areas with heterogeneous land cover, this filtering may combine pixels from areas with different characteristics in ways that are undesirable. We generate two time series: one using the standard approach (all possible pixels), and one where we mask out all but the “stable” pixels at full resolution before any further spatial averaging or filtering.

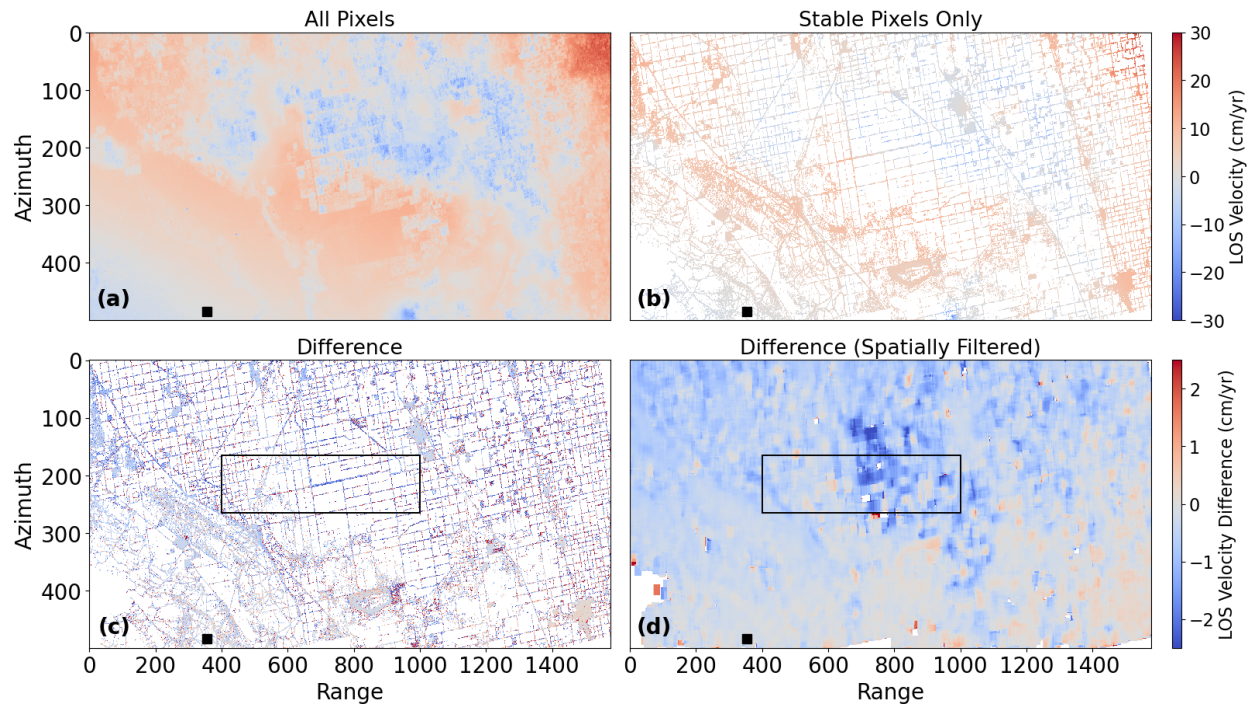


Figure 7. a) Time series inversion using all pixels; **b)** Time series inversion using only stable pixels; **c)** Difference between two time series; **d)** Difference spatially filtered by a factor of

20x20 for visualization purposes. Black box denotes subregion shown in Figure 8a. Reference point shown as a black square.

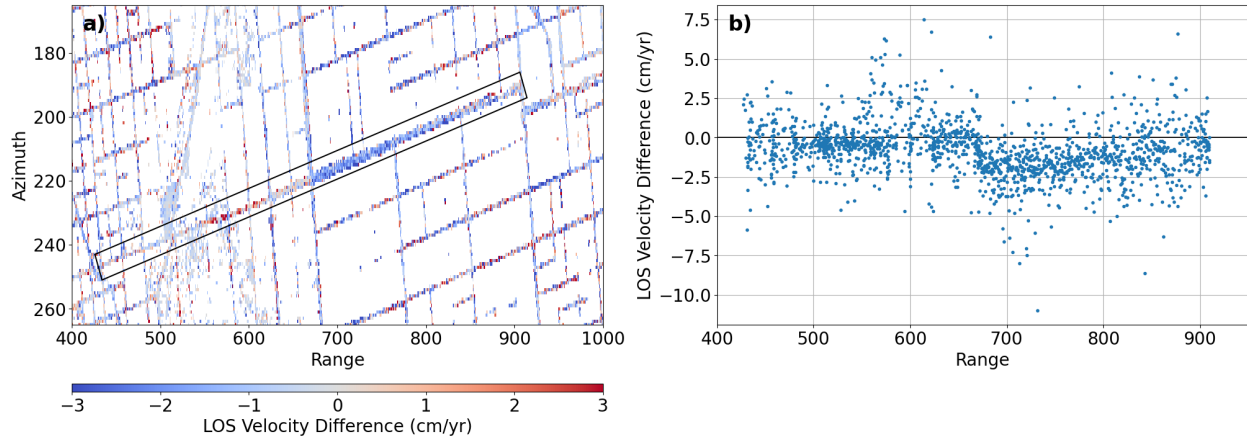


Figure 8. a) Zoomed-in area from Figure 7c of difference between inverting with all pixels and using stable pixels only. Black box outlines pixels shown in (b); **b)** Profile of pixels within black box in (a).

Figure 7 shows the inferred average LOS velocity for both approaches. Peak subsidence is around -30 cm/yr using either method (Figure 7a,b). Figure 7c shows the difference between the two inversions, and Figure 7d spatially filtered for better visualization. Figure 8a focuses on a subregion of the study site, along a road with large fields (cotton for most of the study time interval) to the north and south (Figure 8b). Note the pronounced difference of ~2 cm/yr between the unfiltered/masked and the filtered/unmasked inversions. This difference is due to phase biases in the adjacent fields impacting the inferred phase values along the roads after spatial averaging and filtering. With less spatial averaging, this effect would tend to be smaller, as there would be less averaging of heterogeneous land cover.

4.3.2 Synthetic time series results

The synthetic time series inversion (described in Section 3.3) demonstrates the effect of our observed phase bias over time within each field. We use the same reference pixel as in Section 4.3.1. The inferred LOS velocity varies between individual fields (Figure 9a), with large (cm/yr or more) negative values within the central portion of our study area. Most fields have biases between -2.5 (subsidence) and 1 (uplift) cm/yr (Figure 9b). The largest magnitude biases occur within the artificially drained Tulare Lake, where the majority of cotton fields are located. This is consistent with our observations of cotton having the most distinct phase biases over time. Note that the features visible in Figure 9a are solely due to the observed biases in each individual field. This is in contrast to the rate differences shown in Figure 7c,d, which are

attributable to spatial filtering over heterogeneous land covers (agricultural fields together with stable pixels).

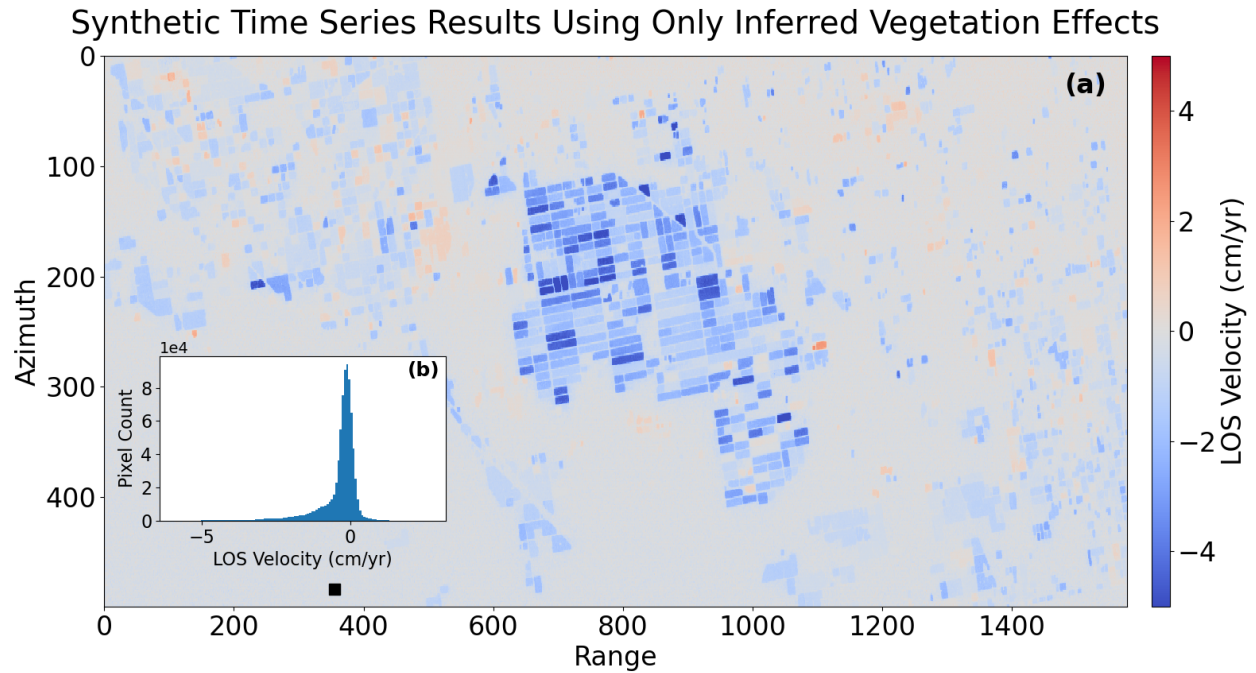


Figure 9. a) LOS velocity inversion of synthetic interferograms. Positive values indicate movement toward the satellite (uplift), and negative values indicate movement away from the satellite (subsidence). Reference point shown as a black square; **b)** Histogram of LOS velocities.

5 Discussion and Conclusion

In agricultural regions where groundwater resources are being heavily utilized, InSAR-derived rates can help with characterizing and managing such resources (e.g., Amelung et al., 1999; Chaussard et al., 2014; Farr, 2016; Gao et al., 2018; Hussain et al., 2022; Kang and Knight, 2023; Motagh et al., 2017; Murray and Lohman, 2018; Neely et al., 2020). However, contributions to the InSAR observations from other factors, such as soil moisture or vegetation characteristics, could bias such observations. In this paper, we examine an approach for mitigating this effect, applied to C-band data from the Sentinel-1 constellation. We also present a method for characterizing how strong the effect on InSAR time series could be. The largest biases we observe occur within cotton fields, although we also observe significant biases and seasonal signals in almond and pistachio orchards. In general, the observed phase bias and NDVI are correlated with each other, suggesting that the bias is due to vegetation effects on the InSAR signal. However, factors like soil moisture may also be correlated with NDVI and may also contribute to the observed biases. Future work that includes the collection of in situ soil moisture measurements, as well as observations at different microwave wavelengths, may help with efforts to separate out vegetation water content from soil moisture effects (e.g., Wig et

al., 2024; Zheng et al., 2022). These effects are likely of interest in their own right, beyond their treatment here as a source of noise in ground deformation studies.

It is likely that some pixels are mislabeled in the CDL database, particularly since the database is only published once a year and may, therefore, miss time periods where a given field is switched from one crop to another. Because we invert for LOS velocity on a field-by-field basis, independent of land cover type, this potential CDL-based issue will not impact our inferred displacement rates over the region (Figures 7-9). However, mislabeling of individual fields will affect our summaries of individual crop types (Figures 5-6), and is only mitigated by the large number of fields that go into each summary.

In general, we observe a bias of $\sim 2\text{--}4$ cm/year of subsidence, both through our comparison of masked vs. unmasked interferograms (Figure 7) and through our modeling of the effect on each individual field over time (Figure 9). The small size of our study region results in some artifacts when compared to previous studies using the same data (e.g., Farr, 2016; Kang and Knight, 2023; Murray and Lohman, 2018; Neely et al., 2020). We attribute the uplift signal we see in the northeast corner of Figure 7a,b to the proximity of the reference point to the subsidence bowl. However, these considerations would not impact either the difference between the masked vs. unmasked time series, or the field-based results. We show that removing pixels that may exhibit suspect behavior, at the highest resolution possible, can help mitigate these biases at low computational cost, without requiring that the user produce more computationally expensive full-resolution displacement maps or perform persistent scatterer analyses (e.g., Ferretti et al., 2000; Hooper et al., 2004).

The peak subsidence rate within the San Joaquin Valley is ~ 30 cm/yr (e.g., Farr, 2016; Kang and Knight, 2023; Lees and Knight, 2024; Murray and Lohman, 2018; Neely et al., 2020), which is an order of magnitude larger than our observed bias. However, while the biases may be insignificant when compared to the signals in this particular region, researchers studying regions with smaller deformation signals or who are interested in analyzing shorter-term variations or seasonality in the subsidence in California, may find it useful to adopt some of the approaches described here.

Acknowledgments

This work was supported by NASA grants: 80NSSC19K1496, 80NSSC23K0721, and 80NSSC22K0460. Copernicus Sentinel-1 data 2019–2021 was retrieved from ASF DAAC 1 October 2021, processed by ESA (<https://www.asf.alaska.edu>). We appreciate the insightful comments of E. Wig, Y. Zheng, and one anonymous reviewer, which greatly improved the manuscript. We also thank Editor C. Jones for her work in efficiently guiding the review process.

Open Research

All raw data used in this analysis are free and open, as is all the software used to prepare analysis-ready data. ESA Sentinel-1a/b data are available through ASF DAAC (<https://search.asf.alaska.edu/>) with a free Earthdata account

(<https://www.earthdata.nasa.gov/>). CDL data are openly available via the CroplandCROS website (<https://croplandcros.scinet.usda.gov/>). Landsat 8 and Sentinel-2 imagery are accessed through Google Earth Engine (<https://earthengine.google.com/>). ISCE2 software and the Sentinel stack processor are available on Github (<https://github.com/isce-framework/isce2>). STRM DEM obtained using the software package sardem on Github (<https://github.com/scottstanie/sardem>). MintPy software is available on Github (<https://github.com/insarlab/MintPy>). Additional code developed by the authors for this analysis is also available on Github (Devlin, 2024) (<https://github.com/kdevlin525/C-band-phase-bias>).

References

- Amelung, F., Galloway, D.L., Bell, J.W., Zebker, H.A., Lacznia, R.J., 1999. Sensing the ups and downs of Las Vegas: InSAR reveals structural control of land subsidence and aquifer-system deformation. *Geology* 27, 483–486. [https://doi.org/10.1130/0091-7613\(1999\)027<0483:STUADO>2.3.CO;2](https://doi.org/10.1130/0091-7613(1999)027<0483:STUADO>2.3.CO;2)
- Asner, G.P., Brodrick, P.G., Anderson, C.B., Vaughn, N., Knapp, D.E., Martin, R.E., 2016. Progressive forest canopy water loss during the 2012–2015 California drought. *Proceedings of the National Academy of Sciences* 113, E249–E255. <https://doi.org/10.1073/pnas.1523397113>
- Bekaert, D.P., Karim, M., Linick, J.P., Hua, H., Sangha, S., Lucas, M., Malarout, N., Agram, P.S., Pan, L., Owen, S.E., Lai-Norling, J., 2019. Development of open-access Standardized
- Bradski, Gary, 2000. The OpenCV Library. *Dr. Dobbs's Journal of Software Tools* 25, 122–125.
- Butler, J.J., Bohling, G.C., Whittemore, D.O., Wilson, B.B., 2020. A roadblock on the path to aquifer sustainability: underestimating the impact of pumping reductions. *Environ. Res. Lett.* 15, 014003. <https://doi.org/10.1088/1748-9326/ab6002>
- Chaussard, E., Wdowinski, S., Cabral-Cano, E., Amelung, F., 2014. Land subsidence in central Mexico detected by ALOS InSAR time-series. *Remote Sensing of Environment* 140, 94–106. <https://doi.org/10.1016/j.rse.2013.08.038>
- Chen, C.W., Zebker, H.A., 2002. Phase unwrapping for large SAR interferograms: statistical segmentation and generalized network models. *IEEE Transactions on Geoscience and Remote Sensing* 40, 1709–1719. <https://doi.org/10.1109/TGRS.2002.802453>
- Copernicus Sentinel-2 (processed by ESA), 2021. MSI Level-2A BOA Reflectance Product. Collection 1. https://doi.org/10.5270/S2_-znk9xsj
- Dall, J., 2007. InSAR Elevation Bias Caused by Penetration Into Uniform Volumes. *IEEE Transactions on Geoscience and Remote Sensing* 45, 2319–2324. <https://doi.org/10.1109/TGRS.2007.896613>
- Devlin, K., 2024. kdevlin525/C-band-phase-bias: December 18, 2024 Release (Version 1.0.0) [Software]. Zenodo. <https://doi.org/10.5281/zenodo.14509589>
- Devlin, K., 2024. kdevlin525/C-band-phase-bias: December 18, 2024 Release (Version 1.0.0) [Software]. Zenodo. <https://doi.org/10.5281/zenodo.14509589>

- De Zan, F., Gomba, G., 2018. Vegetation and soil moisture inversion from SAR closure phases: First experiments and results. *Remote Sensing of Environment* 217, 562–572. <https://doi.org/10.1016/j.rse.2018.08.034>
- Emardson, T.R., Simons, M., Webb, F.H., 2003. Neutral atmospheric delay in interferometric synthetic aperture radar applications: Statistical description and mitigation. *Journal of Geophysical Research: Solid Earth* 108.
- Escriva-Bou, A., Hanak, E., Cole, S., Medellín-Azuara, J., 2023. The Future of Agriculture in the San Joaquin Valley. Public Policy Institute of California.
- Escriva-Bou, A., Hui, R., Maples, S., Medellín-Azuara, J., Harter, T., Lund, J.R., 2020. Planning for groundwater sustainability accounting for uncertainty and costs: An application to California's Central Valley. *Journal of Environmental Management* 264, 110426. <https://doi.org/10.1016/j.jenvman.2020.110426>
- Farr, T.G., 2016. InSAR measurements of subsidence in the Central Valley, California from 2007 - present, in: *Proceedings of EUSAR 2016: 11th European Conference on Synthetic Aperture Radar*. Presented at the Proceedings of EUSAR 2016: 11th European Conference on Synthetic Aperture Radar, pp. 1–3.
- Farr, T.G., Rosen, P.A., Caro, E., Crippen, R., Duren, R., Hensley, S., Kobrick, M., Paller, M., Rodriguez, E., Roth, L., Seal, D., Shaffer, S., Shimada, J., Umland, J., Werner, M., Oskin, M., Burbank, D., Alsdorf, D., 2007. The Shuttle Radar Topography Mission. *Reviews of Geophysics* 45. <https://doi.org/10.1029/2005RG000183>
- Fattahi, H., Agram, P., Simons, M., 2017. A Network-Based Enhanced Spectral Diversity Approach for TOPS Time-Series Analysis. *IEEE Transactions on Geoscience and Remote Sensing* 55, 777–786. <https://doi.org/10.1109/TGRS.2016.2614925>
- Ferretti, A., Prati, C., Rocca, F., 2000. Nonlinear subsidence rate estimation using permanent scatterers in differential SAR interferometry. *IEEE Transactions on Geoscience and Remote Sensing* 38, 2202–2212. <https://doi.org/10.1109/36.868878>
- Gabriel, A.K., Goldstein, R.M., Zebker, H.A., 1989. Mapping small elevation changes over large areas: Differential radar interferometry. *Journal of Geophysical Research: Solid Earth* 94, 9183–9191. <https://doi.org/10.1029/JB094iB07p09183>
- Gao, M., Gong, H., Chen, B., Li, X., Zhou, C., Shi, M., Si, Y., Chen, Z., Duan, G., 2018. Regional Land Subsidence Analysis in Eastern Beijing Plain by InSAR Time Series and Wavelet Transforms. *Remote Sensing* 10, 365. <https://doi.org/10.3390/rs10030365>
- Gleeson, T., Wada, Y., Bierkens, M.F.P., van Beek, L.P.H., 2012. Water balance of global aquifers revealed by groundwater footprint. *Nature* 488, 197–200. <https://doi.org/10.1038/nature11295>
- Goldstein, R.M., Werner, C.L., 1998. Radar interferogram filtering for geophysical applications. *Geophysical Research Letters* 25, 4035–4038. <https://doi.org/10.1029/1998GL900033>
- Gorelick, N., Hancher, M., Dixon, M., Ilyushchenko, S., Thau, D., Moore, R., 2017. Google Earth Engine: Planetary-scale geospatial analysis for everyone. *Remote Sensing of Environment, Big Remotely Sensed Data: tools, applications and experiences* 202, 18–27. <https://doi.org/10.1016/j.rse.2017.06.031>
- Hasan, M.F., Smith, R., Vajedian, S., Pommerenke, R., Majumdar, S., 2023. Global land subsidence mapping reveals widespread loss of aquifer storage capacity. *Nat Commun* 14, 6180. <https://doi.org/10.1038/s41467-023-41933-z>

- Hooper, A., Zebker, H., Segall, P., Kampes, B., 2004. A new method for measuring deformation on volcanoes and other natural terrains using InSAR persistent scatterers. *Geophysical Research Letters* 31. <https://doi.org/10.1029/2004GL021737>
- Hussain, M.A., Chen, Z., Zheng, Y., Shoaib, M., Ma, J., Ahmad, I., Asghar, A., Khan, J., 2022. PS-InSAR Based Monitoring of Land Subsidence by Groundwater Extraction for Lahore Metropolitan City, Pakistan. *Remote Sensing* 14, 3950. <https://doi.org/10.3390/rs14163950>
- Jiang, J., Lohman, R.B., 2021. Coherence-guided InSAR deformation analysis in the presence of ongoing land surface changes in the Imperial Valley, California. *Remote Sensing of Environment* 253, 112160. <https://doi.org/10.1016/j.rse.2020.112160>
- Kang, S., Knight, R., 2023. Isolating the Poroelastic Response of the Groundwater System in InSAR Data From the Central Valley of California. *Geophysical Research Letters* 50, e2023GL103222. <https://doi.org/10.1029/2023GL103222>
- Lees, M., Knight, R., 2024. Quantification of record-breaking subsidence in California's San Joaquin Valley. *Commun Earth Environ* 5, 1–12. <https://doi.org/10.1038/s43247-024-01778-w>
- Mall, N.K., Herman, J.D., 2019. Water shortage risks from perennial crop expansion in California's Central Valley. *Environ. Res. Lett.* 14, 104014. <https://doi.org/10.1088/1748-9326/ab4035>
- Massonnet, D., Rossi, M., Carmona, C., Adragna, F., Peltzer, G., Feigl, K., Rabaut, T., 1993. The displacement field of the Landers earthquake mapped by radar interferometry. *Nature* 364, 138–142. <https://doi.org/10.1038/364138a0>
- Motagh, M., Shamshiri, R., Haghshenas Haghighi, M., Wetzel, H.-U., Akbari, B., Nahavandchi, H., Roessner, S., Arabi, S., 2017. Quantifying groundwater exploitation induced subsidence in the Rafsanjan plain, southeastern Iran, using InSAR time-series and in situ measurements. *Engineering Geology* 218, 134–151. <https://doi.org/10.1016/j.enggeo.2017.01.011>
- Murray, K.D., Lohman, R.B., 2018. Short-lived pause in Central California subsidence after heavy winter precipitation of 2017. *Science Advances* 4, eaar8144.
- Neely, W.R., Borsa, A.A., Silverii, F., 2020. GInSAR: A cGPS Correction for Enhanced InSAR Time Series. *IEEE Trans. Geosci. Remote Sensing* 58, 136–146. <https://doi.org/10.1109/TGRS.2019.2934118>
- Nishikawa, T., Siade, A., Reichard, E., Ponti, D., Canales, A., Johnson, T., 2009. Stratigraphic controls on seawater intrusion and implications for groundwater management, Dominguez Gap area of Los Angeles, California, USA. *Hydrogeology Journal* 17, 1699–1725. <https://doi.org/10.1007/s10040-009-0481-8>
- Petersen-Perlman, J.D., Aguilar-Barajas, I., Megdal, S.B., 2022. Drought and groundwater management: Interconnections, challenges, and policy responses. *Current Opinion in Environmental Science & Health* 28, 100364. <https://doi.org/10.1016/j.coesh.2022.100364>
- Poland, J.F., Lofgren, B.E., Ireland, R.L., Pugh, R.G., 1975. Land Subsidence in the San Joaquin Valley, California, As of 1972. *Geological Survey Professional Paper* 437-H.

- Richey, A.S., Thomas, B.F., Lo, M.-H., Reager, J.T., Famiglietti, J.S., Voss, K., Swenson, S., Rodell, M., 2015. Quantifying renewable groundwater stress with GRACE. *Water Resources Research* 51, 5217–5238. <https://doi.org/10.1002/2015WR017349>
- Rohde, M.M., Albano, C.M., Huggins, X., Klausmeyer, K.R., Morton, C., Sharman, A., Zaveri, E., Saito, L., Freed, Z., Howard, J.K., Job, N., Richter, H., Toderich, K., Rodella, A.-S., Gleeson, T., Huntington, J., Chandanpurkar, H.A., Purdy, A.J., Famiglietti, J.S., Singer, M.B., Roberts, D.A., Caylor, K., Stella, J.C., 2024. Groundwater-dependent ecosystem map exposes global dryland protection needs. *Nature* 632, 101–107. <https://doi.org/10.1038/s41586-024-07702-8>
- Rosen, P.A., Gurrola, E., Sacco, G.F., Zebker, H., 2012. The InSAR scientific computing environment, in: *EUSAR 2012; 9th European Conference on Synthetic Aperture Radar*. Presented at the EUSAR 2012; 9th European Conference on Synthetic Aperture Radar, pp. 730–733.
- Tymofeyeva, E., Fialko, Y., Jiang, J., Xu, X., Sandwell, D., Bilham, R., Rockwell, T.K., Blanton, C., Burkett, F., Gontz, A., Moafipoor, S., 2019. Slow Slip Event On the Southern San Andreas Fault Triggered by the 2017 M8.2 Chiapas (Mexico) Earthquake. *Journal of Geophysical Research: Solid Earth* 124, 9956–9975. <https://doi.org/10.1029/2018JB016765>
- USDA NASS, 2021. Cropland Data Layer: United States Department of Agriculture (USDA) National Agricultural Statistics Service (NASS) [WWW Document]. USDA NASS Marketing and Information Services Office, Washington, D.C. URL <https://croplandcros.scinet.usda.gov/> (accessed 10.1.21).
- Wada, Y., van Beek, L.P.H., van Kempen, C.M., Reckman, J.W.T.M., Vasak, S., Bierkens, M.F.P., 2010. Global depletion of groundwater resources. *Geophysical Research Letters* 37. <https://doi.org/10.1029/2010GL044571>
- Wig, E., Michaelides, R., Zebker, H., 2024. Fine-Resolution Measurement of Soil Moisture From Cumulative InSAR Closure Phase. *IEEE Transactions on Geoscience and Remote Sensing* 62, 1–15. <https://doi.org/10.1109/TGRS.2024.3399069>
- Yunjun, Z., Fattahi, H., Amelung, F., 2019. Small baseline InSAR time series analysis: Unwrapping error correction and noise reduction. *Computers & Geosciences* 133, 104331. <https://doi.org/10.1016/j.cageo.2019.104331>
- Zebker, H.A., Villasenor, J., 1992. Decorrelation in interferometric radar echoes. *IEEE Trans. Geosci. Remote Sensing* 30, 950–959. <https://doi.org/10.1109/36.175330>
- Zheng, Y., Fattahi, H., Agram, P., Simons, M., Rosen, P., 2022. On Closure Phase and Systematic Bias in Multilooked SAR Interferometry. *IEEE Transactions on Geoscience and Remote Sensing* 60, 1–11. <https://doi.org/10.1109/TGRS.2022.3167648>
- Zwieback, S., Hensley, S., Hajnsek, I., 2015. Assessment of soil moisture effects on L-band radar interferometry. *Remote Sensing of Environment* 164, 77–89. <https://doi.org/10.1016/j.rse.2015.04.012>

